This is the accepted version of the following article: Sun, P., Jin, Y., Yin, Y., Wu, C., Song, C., Feng, Y., Zhou, P., Qin, X., Niu, Y., Liu, Q., Zhang, J., Wang, Z., Hao, X., Achieving Extreme Pressure Resistance to Liquids on a Super-Omniphobic Surface with Armored Reentrants. Small Methods 2023, Early View, 2201602, which has been published in final form at https://doi.org/10.1002/smtd.202201602. This article may be used for non-commercial purposes in accordance with the Wiley Self-Archiving Policy [olabout.wiley.com/WileyCDA/Section/id- 820227.html].

Achieving extreme pressure resistance to liquids on a super-omniphobic surface with armored reentrants

Pengcheng Sun, Yuankai Jin, Yingying Yin, Chenyang Wu, Chuanhui Song, Yawei Feng, Peiyang Zhou, Xuezhi Qin, Yusheng Niu, Qiankai Liu, Jie Zhang, Zuankai Wang[*] and *Xiuqing Hao*[*]

P. Sun, Y. Niu, Q. Liu, J. Zhang, Prof. X. Hao
College of Mechanical and Electrical Engineering, Nanjing University of Aeronautics and Astronautics, Nanjing, Jiangsu, P. R. China

P. Sun, Dr. Y. Jin, Y. Yin, C. Wu, Dr. Y. Feng, P. Zhou, X. Qin
Department of Mechanical Engineering, City University of Hong Kong, Hong Kong, P. R. China

Dr. C. Song
Department of Oral and Maxillofacial Surgery, Nanjing Stomatological Hospital, Medical School of Nanjing University, No. 30 Zhongyang Road, Nanjing, 210008, P. R.China.

Prof. Z. Wang
Department of Mechanical Engineering, City University of Hong Kong, Hong Kong, P. R. China
Department of Mechanical Engineering, The Hong Kong Polytechnic University, Hong Kong, P. R. China

Corresponding authors: Prof. X. Hao and Prof. Z. Wang
E-mail: xqhao@nuaa.edu.cn; zuanwang@polyu.edu.hk

Abstract

Both static liquid repellency and pressure resistance are essential for high-performance super-omniphobic surfaces. However, these two merits appear almost mutually exclusive in conventional designs because of their conflicting structural demands: Static liquid repellency generally necessitates minimal solid-liquid contact, which in turn inevitably undercuts the surface's ability to resist liquid invasion exerted by the elevated pressure. Here, inspired by the *Springtail*, these two merits can be simultaneously realized by structuring surfaces at two different size scales, with a micrometric reentrant structure providing static liquid repellency and a nanometric reentrant structure providing pressure resistance, which dexterously avoids the dilemma of their structural conflicts. The nanometric reentrants are densely packed on the micrometric ones, serving as "armor" that prevents liquids invasion by generating multilevel energy barriers, thus naming our surface as the armored reentrants (AR) surface. Our AR surface could repel liquids with low surface tensions, such as silicone oil (21 *mN/m*), and simultaneously resist great pressure from the liquids, exemplified by enduring the impact of low-surface-tension liquids under a high weber number (> 400), the highest-pressure resistance ever reported. With its scalable fabrication and enhanced performance, we anticipate that our design could extend the application scope of liquid-repellent surfaces toward industrial settings.

Keywords

Super-omniphobic surface, pressure resistance, laser machining, bio-inspired surface, structural hierarchy

1. Introduction

Maintaining a robust liquid-repellency state on a super-omniphobic surface, especially under extreme environments involving elevated pressure, such as high-pressure liquid impact, is imperative for both fundamental research[1] and a myriad of practical applications, such as anti-icing on airplanes[2], energy conservation on submarines[3] as well as self-cleaning on electronic devices[4]. Such a robust liquid-repellency state favors the Cassie-Baxter wetting state[5], which can be guaranteed by surfaces' static liquid repellency and pressure resistance. However, achieving these two merits simultaneously on one super-omniphobic surface has proved to be a daunting challenge due to their conflicting demands on the surface structures[6]. High static repellency requires sparse surface structures to achieve a minimal solid-liquid contact area, which in turn inevitably impairs the surface's resistance to the elevated liquid pressure, posing the possibility of liquid invasion and associated wetting collapse, exemplified by the Cassie-to Wenzel transisition[7].

The past several years have witnessed a surge of techniques for high-performance super-omniphobic surfaces, with extensive efforts in exploring an effective design to achieve high static repellency and extreme pressure resistance[8]. One typical strategy is to structure the surfaces with the reentrant[6a, 8f, 8g, 9], an elegant structure featured with an architecture narrowing below the surface. Such a structure displays strong static liquid repellency by taking advantage of the energy barrier generated by its unique geometrical property[9b, 9c], but it has weak pressure resistance to even gentle pressure. To enhance the pressure resistance of super-omniphobic surfaces, a *Springtail*-inspired hierarchical system was brought to stage[10]. Such a system can tolerate high liquid pressure due to the cooperation of the micrometric wrinkle and nanometric doubly reentrants[11]. However, this system fails to tolerate the impact from liquids with low intrinsic contact angles, such as silicone oil. In addition, this system requires a denser arrangement of nanometric reentrants to ensure its pressure resistance but appears almost impossible on its fabrication side[12], suggesting its scalability and feasibility are missing.

Here, inspired by the hierarchical system found on the *Springtail*, we design an armored reentrants (AR) surface that displays both high static liquid repellency and extreme pressure resistance, with performances superior to all the previously reported super-omniphobic surfaces. The AR surface consists of micrometric globular-shaped reentrants, with nanometric reentrants densely packed on them. The nanometric reentrant is reminiscent of armors that prevent the invasion of liquids by generating multilevel and stepwise energy barriers. As a critical result, the liquid-repellent AR surface could repel silicone oil with a surface tension of 21 *mN/m* and simultaneously endure the alcohol and ethylene glycol droplets impact by an extreme high weber number (400), which represents the highest-pressure resistance ever reported. On the fabrication side, we propose a new one-step method to fabricate the AR surface on a large scale (200 *mm*×200 *mm* at a time) by using an economical yet largely overlooked nanosecond laser[13]. This method allows for a much easier manufacturing process, lower cost, and greater robustness than the previous strategies in fabricating super-omniphobic surfaces, showing promising prospects in industrial applications.

2. Results and Discussions

2.1 Design and fabrication

Figure 1a shows the super-omniphobic cuticle of the *Springtail*, which displays both high static liquid repellency and excellent pressure resistance to liquids[10]. Such superior liquid repellency originates from its two-size-scaled structures, namely a hierarchical system, comprising micrometric wrinkles and nanometric reentrants (Figure 1a). Inspired by this hierarchical system and based on the fact that a denser arrangement of nanometric reentrants yields a higher-pressure resistance[6c, 10, 12], we design an armored reentrant (AR) surface, featured with hierarchical scales, consisting micrometric globular-shaped reentrants that have nanometric reentrants densely decorated on them, as shown in Figure 1b and Figure S1. At the same time, we also design a control surface with bare micrometric globular reentrants (Figure 1c). Note that the micrometric globular reentrant of the AR surface could synergistically work with the nanometric reentrants, which is otherwise impossible for previously used structures, such as the wrinkle structure used in the traditional hierarchical systems and the T-shaped reentrant used in the doubly- or triply-reentrant (Note S1, Figures S2 to S4).

Meaningfully, we fabricate the AR structures by using an economical yet largely overlooked nanosecond laser based on our newly proposed “digging effect”, which is discussed in detail in Note S2 and Figures S5-S7. Our fabrication method is universal to various materials, ranging from traditional metallic materials, such as copper, to a series of difficult-to-cut materials, such as cermet (Figure S5), and allows for mass production of the AR structures (200 *mm*×200 *mm*), which holds promising application prospects beyond those traditional manufacturing techniques, such as 3D nano-printing and lithography.

2.2 Static repellency

We first demonstrate the static liquid repellency of the AR and control surface. As depicted in Figure 1d, the AR surface is super-repellent to various liquids, including water (with an intrinsic contact angle θ_Y of 87°), ethanol (θ_Y=55°), silicone oil (θ_Y=0°), and many other low surface tension liquids (Figure S8), allowing them to bead with high contact angles (Figure 1e) and slide with low sliding angles (Figure 1f). The control surface, by contrast, fails to repel liquids of low θ_Y (<55°), characterized by either wicking or low contact angles of these liquids.

To reveal how the design of the AR surface could facilitate its improved static liquid repellency, we analyzed the evolution of the free energy after a liquid droplet is deposited on the AR surface (Note S3, Figure S9). Benefitting from the nanometric reentrants, the AR surface could generate a preferred energy barrier for liquids, even for liquids with extremely low θ_Y, akin to a suspension 'force' (F>0, Figure 1g) to suspend the liquids[9c]. Hereafter, the energy barriers that prevent the collapse of liquids are called forces due to their force-like role. The control surface, by contrast, can only generate such a preferred suspension force for liquids of high θ_Y, which agrees well with the observations in Figure 1e. For the liquids of low θ_Y, the control surface doesn't simply lose the ability to generate suspension forces; what's worse, it generates a drag force that drags the liquids towards the bottom of the surface and accelerates their wetting collapses (F<0, Figure 1h), which is also consistent with our observations in Figure 1e.

2.3 Pressure resistance under liquid impact

Another imperative parameter for a high-performance super-omniphobic surface is its pressure resistance, which can be qualified from two aspects: high-pressure liquid impact and inner elevated Laplace pressure[8b, 14]. We start from impacting 20 vol% alcohol solution (θ_Y=55°) by using a weber number (We) of 30 ($We=\rho U^2 d/\gamma$, for density ρ, impacting velocity U, droplet diameter d). Alcohol is used because this liquid adopts almost identical adhesions and contact angles on the AR and control surfaces (Figure 1g and Figure S10, Note S4). Surprisingly, despite their identical static liquid repellency, the AR and control surface show distinct repellency to the impacting alcohol droplets: The AR surface allows it to bounce four times (Figure 2a and Video S1), whereas the control surface directly captures it and inhibits its bouncing (Figure 2b and Video S1). This observation raises a very puzzling question: How can two surfaces with the same static liquid repellency lead to such a distinct pressure resistance? To answer this question, we resort to *COMSOL* simulation to reveal the interfacial hydrodynamics during liquid impact. As shown in Figure 2c and Figure

2d, the control surface fails to lock the air when an alcohol droplet impacts on it and the alcohol droplet breaks into the structures, causing undesired wetting collapse. The AR surface, by contrast, could maintain a stable air cushion beneath the droplet, preventing the droplet from breaking into the structures and hence, balancing the high pressure from the liquid impact.

To demonstrate how far our AR surface has achieved in the improved pressure resistance, we impact the surface by using highly wetting liquids, including alcohol solution (θ_Y=55°) and ethylene glycol (θ_Y=15°) through an extremely high *We*. The AR surface allows the impacting alcohol (Figure 2e, Video S2) and ethylene glycol (Video S3) to bounce off the surface under *We*=400. This is the highest *We* our experimental setup could achieve, and the highest-pressure resistance ability ever reported (Figure 2f)[6a, 8b, 8c, 8f, 8h, 10], even far surpassing all the hierarchical systems (highlighted in the green area in Figure 2f). Meaningfully, the AR surface's pressure resistance is universal, regardless of the volume and θ_Y of the liquid. As shown in Figure 2g and Video S4, the AR surface is still effective when impacted by a stream of (30 *ml*) silicone oil with an extremely low θ_Y (~0°) from a height of 50 mm.

2.4 Pressure resistance under liquid evaporation

We then investigated the pressure resistance of the AR surface in stabilizing the preferred Cassie state under liquid evaporation by taking advantage of the fact that an evaporating droplet with a shrinking droplet size results in monotonically increased inner Laplace pressure (P=4γ/d, where P is the Laplace pressure). Generally, the stability of the Cassie-Baxter state during liquid evaporating can be characterized by confocal microscopy[8b, 14]. However, this equipment is ineffective for those surfaces with opaque and disorderly distributed structures. Here, we proposed a new method to visually characterize the stability of the Cassie-Baxter state on the AR surface, which is based on a widely explored effect—the coffee-ring effect (Note S5, Figures S10, S11). Briefly, the stability of the Cassie-Baxter state can be judged by the final arrangement of the tracer beads suspended in the shrinking water: a Cassie-to-Wenzel transition would result in the formation of a coffee ring, while a stable Cassie-Baxter state would suppress this coffee ring, leading to the formation of a compact that aggregates at the center of the evaporated liquid drop. Based on this method, we conducted the evaporating experiment, and the results are shown in Figure 3a and Figure 3b. As expected, the Cassie-Baxter state on the AR surface is stable, as the tracer beads are left to be compact. In contrast, the Cassie-Baxter state collapses on the control surface, as evidenced by the formation of a coffee ring.

The improved pressure resistance in resisting the wetting transition, as observed on the AR surface during water evaporation, could also be further quantified from the liquid hydrodynamics. Figure 3c shows the d, the final contact angle (θ), and the P of the water droplet during the evaporation process. At the initial stage (0 min-22 min), the d decreases on both the AR and control surfaces, which agrees well with the observation (Figures 3a, 3b), suggesting that both surfaces are in the Cassie-Baxter wetting state. However, as the evaporating process continues (after 22 min), two distinct scenarios occur: On the control surface, the d ceases to decrease, as manifested by the unshrinking droplet in Figure 3b, suggesting the Cassie has transited to the Wenzel. In contrast, the d on the AR surface continuously decreases till the end of the evaporation process, indicating that the Cassie state is well maintained on the AR surface. The improved pressure resistance of the AR surface in resisting the wetting transition could also be manifested from θ. On the control surface, the θ approaches 0° at the end of the evaporating process. However, on the AR surface, the θ manifests a significantly higher value, as supported by the Cassie state. To directly quantify the pressure resistance of the AR surface, we calculate the evolution of P[14]. On the control surface, the P can increase to 450 Pa before the Cassie transits to Wenzel. In striking contrast, on the AR surface, the P could rise to 1100 Pa, and simultaneously, the AR surface still maintains a stable Cassie state, confirming the pressure resistance of the AR surface in response to the inner elevated Laplace pressure.

We resort to force analysis to reveal how the design of the AR surface could facilitate its pressure resistance. The stepwise increased force (F) with liquid impacting on the AR surface is derived in Note S3 and is schematically shown in Figure 3d. During the invasion of liquids, the F first gradually increases until it reaches the maximum value (F_{max1}), as shown in Figure 3e. Then F undergoes a sudden increase as the liquid advances from the top nanometric reentrant to its neighboring lower one ($D_{1\rightarrow 2}$). Afterward, similarly, the F gradually increases again until the second maximum value (F_{max2}) and undergoes a sudden increase as the liquid advances to the next nanometric reentrant ($D_{2\rightarrow 3}$). The cycle will continue until F is strong enough to balance the pressure imposed by the liquids. Given the dense nanometric reentrants, the F can be well guaranteed on the AR surface. On the control surface, however, the F is a drag force ($F<0$) that will collapse the surface wetting. And with the liquid invading, the F continuously increases, further worsening the surface wetting state, inevitably leading to the Cassie-to-Wenzel transition. It is worth noting that although the F on the control surface can be a suspension force for those liquids with high θ_Y (Figure 1g), such as the alcohol, it can be easily overcome by the high pressure from liquid impact (Figure S12), leading to a devastating wetting collapse.

2.5 Robustness and applications

Conventional perception may have it that a topologically exquisite surface must be mechanically vulnerable to external loads, such as intense friction. However, our AR surface is structurally sophisticated yet mechanically robust. For instance, the AR surface is functionally uncompromised following intense knife scratching (Figure 4a and Video S4), with scratching width of 100 µm, which is otherwise impossible for its counterparts[8b]. Such a mechanical robustness of the AR surface originates from its structural self-similarity, as evidenced by the presence of the armor after scratching, which are seamlessly lying at the region of the scratch (Figure S13) and supporting the local repellency. In addition, the AR surface is firmly bond by its nanometric reentrants, which is strong enough to endure the ultrasonic cleaning (Figure 4b). The binding force of the armor with the AR surface is then further qualified from the AFM scratching test, measuring up to be 100 *mN* (Figure 4c), 67 % higher than other methods[15]. Meanwhile, our AR surface also displays superior chemical robustness (*pH*=3 etching for 12 hours), high thermal stability (300 °C), and prolonged lifespan (120 days and more), as shown in Figure S14, which implies the potential of the AR surface in industrial settings.

We further explored the robust repellency of the AR surface considering its static liquid-repellency and pressure resistance. For instance, based on the static liquid repellency, the AR surface could be applied to the oil manipulation (SI Note 6, Figure 4d, Video S5), wherein the oil droplet freely slides on the AR surface along a predefined track. Additionally, considering its pressure resistance to evaporating liquid droplet, the AR surface could also be adopted to achieve the anti-bacterial purpose by preventing the liquid containing bacteria from breaking into the surface structures. We deposit a liquid droplet containing pathogenic bacteria *Staphylococcus aureus* on the AR surface for 18 hours and found that the AR surface is effective in preventing this bacterium from colonizing (SI Note 6, Figure 4e), evidenced by the significantly subtracted optical density at a wavelength of 600 nm (O. D. 600), indicating the potential of the AR surface in biological and medical applications.

3. Conclusion

In summary, by mimicking and prospering the hierarchical system found on the *Springtail*, we designed a super-omniphobic AR surface with both static repellency and pressure repellence by marrying the reentrants from two size scales. On the fabrication side, we proposed a new “digging effect”, which is based on an economical yet largely underappreciated nano-second laser, significantly propelling the product scalability and versatility of high-performance super-omniphobic surfaces. Our AR surface dexterously circumvents the dilemma of conflicting structural demands faced by conventional liquid-repellent surfaces, achieving the highest record pressure resistance ability while accommodating a high static liquid repellency, which is otherwise impossible on its counterparts. Our study also reveals the multilevel and stepwise pressure resistance mechanism triggered by the armored reentrants, providing new insight into the fundamental understanding of the design of the robust liquid-repellent surface. Leveraging the collectively boosted performance, we envision that our design could enrich the spectrum of high-performance super-omniphobic surfaces and open a new avenue for its applications toward ultimate industrial settings.

Associated Content

Supporting Information

The supporting information includes the Materials and Methods, Supporting Notes S1−S6, and Supplementary Figures. Supporting Notes include the role of globular-shaped reentrant in liquid repellency of the AR surface, the fabrication of the AR structures, the suspension force generated by the AR surface for balancing the invading liquids, the adhesion of the AR surface, the rationalization of the coffee-ring based method in characterizing the stability of the Cassie-Baxter state, the applications of the AR surface.

Video S1: Comparison of the pressure resistance of the AR surface (left) and the control surface (right) tested by impacting an alcoholic liquid drop on the surfaces under the weber number of 30. The AR surface allows the liquid drop to bounce four times before resting while the control surface directly pins the liquid drop.

Video S2: Demonstration of the pressure resistance of the AR surface tested by impacting an alcoholic liquid drop on the surfaces under an extremely high weber number of 400.

Video S3: Demonstration of the pressure resistance of the AR surface tested by impacting an ethylene glycol drop on the surfaces under an extremely high weber number of 400.

Video S4: The mechanical robustness of the AR surface. After knife scratching, despite with notable scratches on the surface, the AR surface still allows the silicone oil to slide freely on the surface.

Video S5: Oil manipulation achieved by the AR-based wettability pattern. The wettability pattern includes the super-oleophilic S-shaped track, which is achieved by laser etching, and a super-omniphobic background with the AR structures.

Acknowledgements

The authors acknowledge financial support from the National Natural Science Foundation of China (Grant No. 51875285), Natural Science Foundation of Jiangsu Province (Grant No. BK20190066), College Young Teachers Fund of the Fok Ying Tung Education Foundation (Grant No. 171045, 20193218210002), Fundamental Research Funds for the Central Universities (Grant No. NE2020005), and the Research Grants Council of Hong Kong (Grant Nos. 11213320 and C1006–20WF).

P. Sun and Y. Jin contribute equally to this work.

Data Availability

The data that supports the findings of this study are available within the article.

Conflict of Interest

The authors declare no conflict of interest.

References

[1] a) H. Chen, P. Zhang, L. Zhang, H. Liu, Y. Jiang, D. Zhang, Z. Han, L. Jiang, *Nature* **2016**, 532, 85; b) F. Chen, Y. Wang, Y. Tian, D. Zhang, J. Song, C. R. Crick, C. J. Carmalt, I. P. Parkin, Y. Lu, *Chem. Soc. Rev.* **2022**; c) J. V. Timonen, M. Latikka, L. Leibler, R. H. Ras, O. Ikkala, *Science* **2013**, 341, 253; d) Y. Jin, C. Wu, P. Sun, M. Wang, M. Cui, C. Zhang, Z. Wang, *Droplet* **2022**, 1, 92; e) S. Hu, X. Cao, T. Reddyhoff, X. Ding, X. Shi, D. Dini, A. J. Demello, Z. Peng, Z. Wang, *Droplet* **2022**, 1, 48.

[2] a) M. J. Kreder, J. Alvarenga, P. Kim, J. Aizenberg, *Nat. Rev. Mate.* **2016**, 1; b) C. Chen, Z. Tian, X. Luo, G. Jiang, X. Hu, L. Wang, R. Peng, H. Zhang, M. Zhong, *Chem. Eng. J.* **2022**, 450; c) K. L. Wilke, D. J. Preston, Z. Lu, E. N. Wang, *ACS Nano* **2018**, 12, 11013.

[3] a) R. J. Daniello, N. E. Waterhouse, J. P. Rothstein, *Phys. Fluids* **2009**, 21; b) M. Xu, G. Sun, C. J. Kim, *Phys. Rev. Lett.* **2014**, 113, 136103; c) Y. Xiang, S. Huang, T. Y. Huang, A. Dong, D. Cao, H. Li, Y. Xue, P. Lv, H. Duan, *Proc. Natl. Acad. Sci. U S A* **2020**, 117, 2282; d) D. P. Erdosy, M. B. Wenny, J. Cho, C. DelRe, M. V. Walter, F. Jimenez-Angeles, B. Qiao, R. Sanchez, Y. Peng, B. D. Polizzotti, M. O. de la Cruz, J. A. Mason, *Nature* **2022**, 608, 712; e) Y. Fu, J. Jiang, Q. Zhang, X. Zhan, F. Chen, *J. Mater. Chem. A* **2017**, 5, 275; f) Z. Tong, L. Song, S. Chen, J. Hu, Y. Hou, Q. Liu, Y. Ren, X. Zhan, Q. Zhang, *Adv. Funct. Mater.* **2022**, 32, 2201290.

[4] a) D. C. Leslie, A. Waterhouse, J. B. Berthet, T. M. Valentin, A. L. Watters, A. Jain, P. Kim, B. D. Hatton, A. Nedder, K. Donovan, E. H. Super, C. Howell, C. P. Johnson, T. L. Vu, D. E. Bolgen, S. Rifai, A. R. Hansen, M. Aizenberg, M. Super, J. Aizenberg, D. E. Ingber, *Nat. Biotechnol.* **2014**, 32, 1134; b) M. Sharma, P. K. Roy, J. Barman, K. Khare, *Langmuir* **2019**, 35, 7672; c) M. Villegas, Y. Zhang, N. Abu Jarad, L. Soleymani, T. F. Didar, *ACS Nano* **2019**, 13, 8517; d) Y. C. Jung, B. Bhushan, *ACS nano* **2009**, 3, 4155.

[5] A. Cassie, S. Baxter, *Transactions of the Faraday society* **1944**, 40, 546.

[6] a) T. L. Liu, C.-J. C. Kim, *Science* **2014**, 346, 1096; b) J. Panter, Y. Gizaw, H. Kusumaatmaja, *Sci. adv.* **2019**, 5, eaav7328; c) A. Tuteja, W. Choi, M. Ma, J. M. Mabry, S. A. Mazzella, G. C. Rutledge, G. H. McKinley, R. E. Cohen, *Science* **2007**, 318, 1618; d) A. Tuteja, W. Choi, J. M. Mabry, G. H. McKinley, R. E. Cohen, *Proc. Natl. Acad. Sci. U S A* **2008**, 105, 18200; e) J. H. Kim, T. S. Shim, S. H. Kim, *Adv. Mater.* **2016**, 28, 291.

[7] a) P. Papadopoulos, L. Mammen, X. Deng, D. Vollmer, H. J. Butt, *Proc. Natl. Acad. Sci. U S A* **2013**, 110, 3254; b) P. Lv, Y. Xue, H. Liu, Y. Shi, P. Xi, H. Lin, H. Duan, *Langmuir* **2015**, 31, 1248.

[8] a) D. Wang, Q. Sun, M. J. Hokkanen, C. Zhang, F. Y. Lin, Q. Liu, S. P. Zhu, T. Zhou, Q. Chang, B. He, Q. Zhou, L. Chen, Z. Wang, R. H. A. Ras, X. Deng, *Nature* **2020**, 582, 55; b) J. Sun, P. Zhu, X. Yan, C. Zhang, Y. Jin, X. Chen, Z. Wang, *Appl. Phys. Rev.* **2021**, 8, 031403; c) X. Deng, L. Mammen, H.-J. Butt, D. Vollmer, *Science* **2012**, 335, 67; d) C. Hao, J. Li, Y. Liu, X. Zhou, Y. Liu, R. Liu, L. Che, W. Zhou, D. Sun, L. Li, L. Xu, Z. Wang, *Nat. Commun.* **2015**, 6, 7986; e) H. Zhang, X. Bu, W. Li, M. Cui, X. Ji, F. Tao, L. Gai, H. Jiang, L. Liu, Z. Wang, *Adv. Mater.* **2022**, 34, e2203792; f) S. Pan, R. Guo, M. Bjornmalm, J. J. Richardson, L. Li, C. Peng, N. Bertleff-Zieschang, W. Xu, J. Jiang, F. Caruso, *Nat Mater* **2018**, 17, 1040; g) E. M. Domingues, S. Arunachalam, H. Mishra, *ACS Appl. Mater. Inter.* **2017**, 9, 21532; h) H. Wang, Z. Zhang, Z. Wang, J. Zhao, Y. Liang, X. Li, L. Ren, *Chem. Eng. J.* **2020**, 394.

[9] a) R. N. Wenzel, *Ind. Eng. Chem.* **1936**, 28, 988; b) R. Hensel, R. Helbig, S. Aland, H. G. Braun, A. Voigt, C. Neinhuis, C. Werner, *Langmuir* **2013**, 29, 1100; c) Y. Kaufman, S.-Y. Chen, H. Mishra, A. M. Schrader, D. W. Lee, S. Das, S. H. Donaldson, J. N. Israelachvili, *J. Phys. Chem. C* **2017**, 121, 5642; d) Y. Yang, Y. Zhang, Y. Hu, G. Li, C. Zhang, Y. Song, L. Li, C. Ni, N. Dai, Y. Cai, J. Li, D. Wu, J. Chu,

Nano Lett. **2021**, 21, 9301; e) J. Wei, B. Li, N. Tian, J. Zhang, W. Liang, J. Zhang, *Adv. Funct. Mater.* **2022**, 32, 202206014; f) S. M. Kang, J. S. Choi, *Small* **2020**, 16, e1904612.

[10] G.-T. Yun, W.-B. Jung, M. S. Oh, G. M. Jang, J. Baek, N. I. Kim, S. G. Im, H.-T. Jung, *Sci. Adv.* **2018**, 4, eaat4978.

[11] L. Gao, T. J. McCarthy, *Langmuir* **2006**, 22, 2966.

[12] A. Hemeda, M. Gad-el-Hak, H. V. Tafreshi, *Phys. Fluids* **2014**, 26, 082103.

[13] a) F. Chen, D. Zhang, Q. Yang, J. Yong, G. Du, J. Si, F. Yun, X. Hou, *ACS Appl. Mater. interfaces* **2013**, 5, 6777; b) M. K. Tiwari, I. S. Bayer, G. M. Jursich, T. M. Schutzius, C. M. Megaridis, *ACS Appl. Mater Interfaces* **2010**, 2, 1114.

[14] X. Li, J. Yang, K. Lv, P. Papadopoulos, J. Sun, D. Wang, Y. Zhao, L. Chen, D. Wang, Z. Wang, X. Deng, *Natl. Sci. Rev.* **2021**, 8, nwaa153.

[15] a) Q. Li, L. Cheng, J. Shen, J. Shi, G. Chen, J. Zhao, J. Duan, G. Liu, W. Jin, *Sep. Purif. Technol.* **2017**, 178, 105; b) D. A. Banerjee, A. J. Kessman, D. R. Cairns, K. A. Sierros, *Surf. Coat. Technol.* **2014**, 260, 214; c) C. E. Nwankire, G. Favaro, Q.-H. Duong, D. P. Dowling, *Plasma Processes Polym.* **2011**, 8, 305.

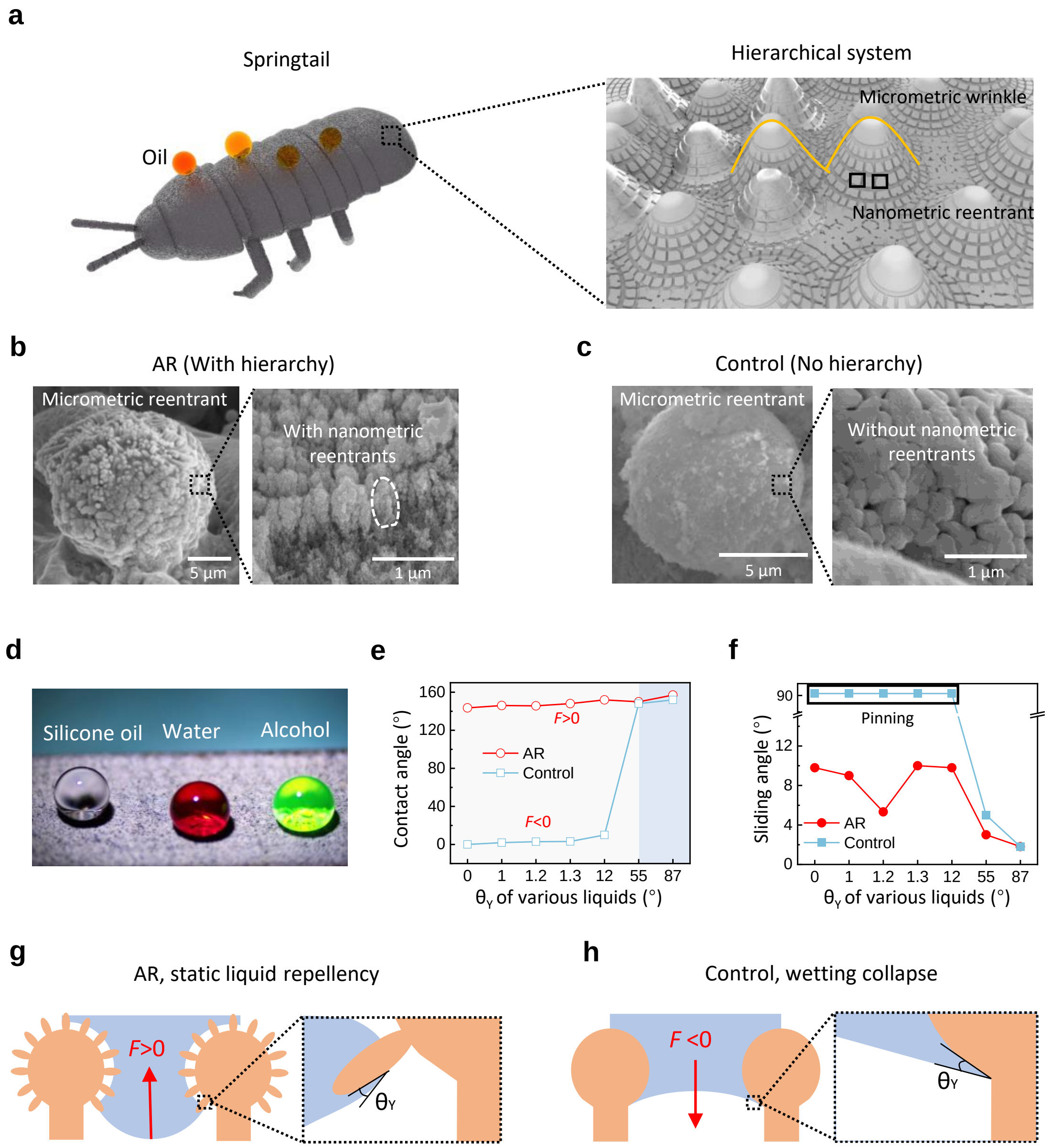

Figure 1. *Springtail*-inspired design of the AR surface and its static liquid repellence. (a) Schematics of a *Springtail*. Zoom-in schematically describes the topology of its super-omniphobic cuticle, comprising micrometric wrinkles (highlighted by the black curves) and the nanometric reentrants (highlighted by the black frames). (b, c) SEM of the *Springtail*-inspired AR surface (b) and the control surface (c), differing only by the presence of nanometric reentrants. The white dashed lines highlight a nanometric reentrant, with an architecture narrowing blow the surface. (d, e) The F generated by the AR surface (d) and control surface (e) to the liquids of low θ_Y. The F generated by the AR surface serves as a suspension force ($F>0$) that supports the wetting, whereas the F generated by the control surface serves as a drag force ($F<0$) that collapses the wetting. (f) Optical image describing the liquids of different θ_Y resting on the AR surface in near-spherical shapes. (g) Contact angles of various liquids on the AR and control surface. (h) Sliding angles of various liquids on the AR and control surface.

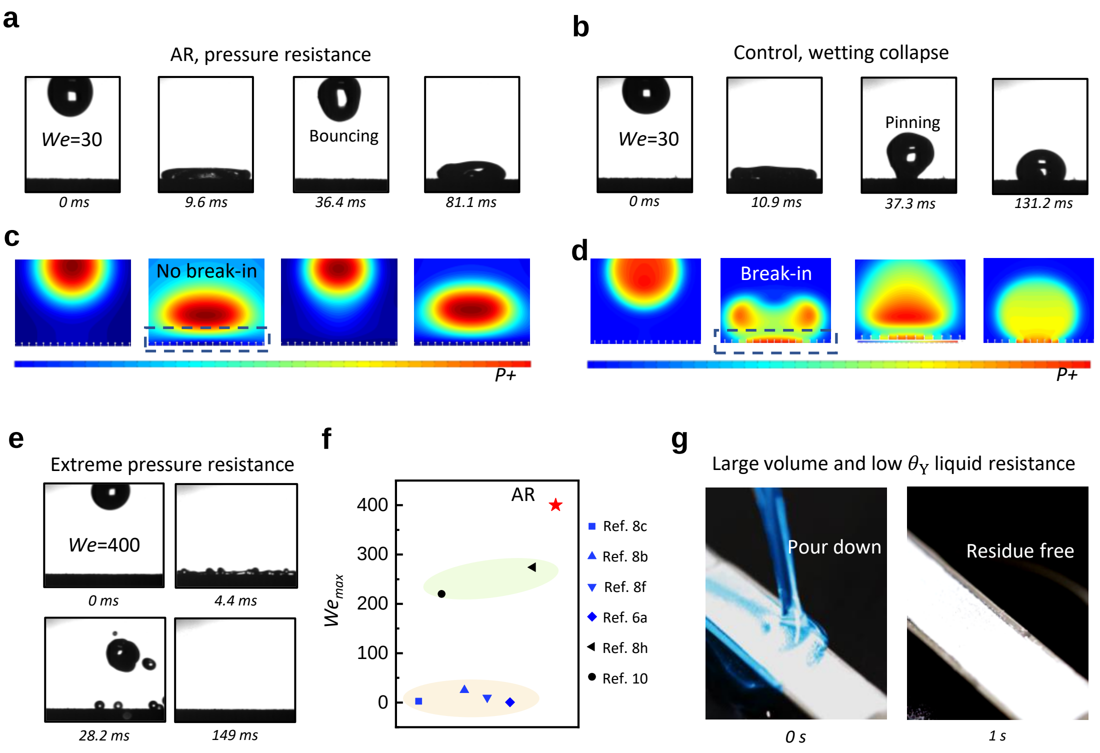

Figure 2. Pressure resistance of the AR surface tested under high-pressure liquid impact. (a, b) Selected snapshots showing a liquid droplet (alcohol solution, 20 vol%, θ_Y=55°) impacting on the AR surface (a) and the control surface (b). The experiment was conducted under *We*=30 in both cases, with an impact velocity of 0.8 m/s, corresponding to a 32.6 mm height. (c, d) Simulation results of the liquid impact experiment on the AR surface (c) and the control surface (d), with experimental conditions identical to the experiments: We=30, controlled by endowing the liquid droplet (alcohol solution, 20 vol%, θ_Y=55°) with an impact velocity of 0.8 m/s from a height of 3 mm. The pressure bars are not to scale. (e) Selected snapshots of liquid impacting the AR surface under *We*=400. (f) Comparison of the maximum allowed *We* on the AR surface and previously reported designs, including designs with (green area) and without hierarchical structures (pink area). (g) Snapshots of 30 *mL* silicone oil (θ_Y=0°) pouring on the AR surface.

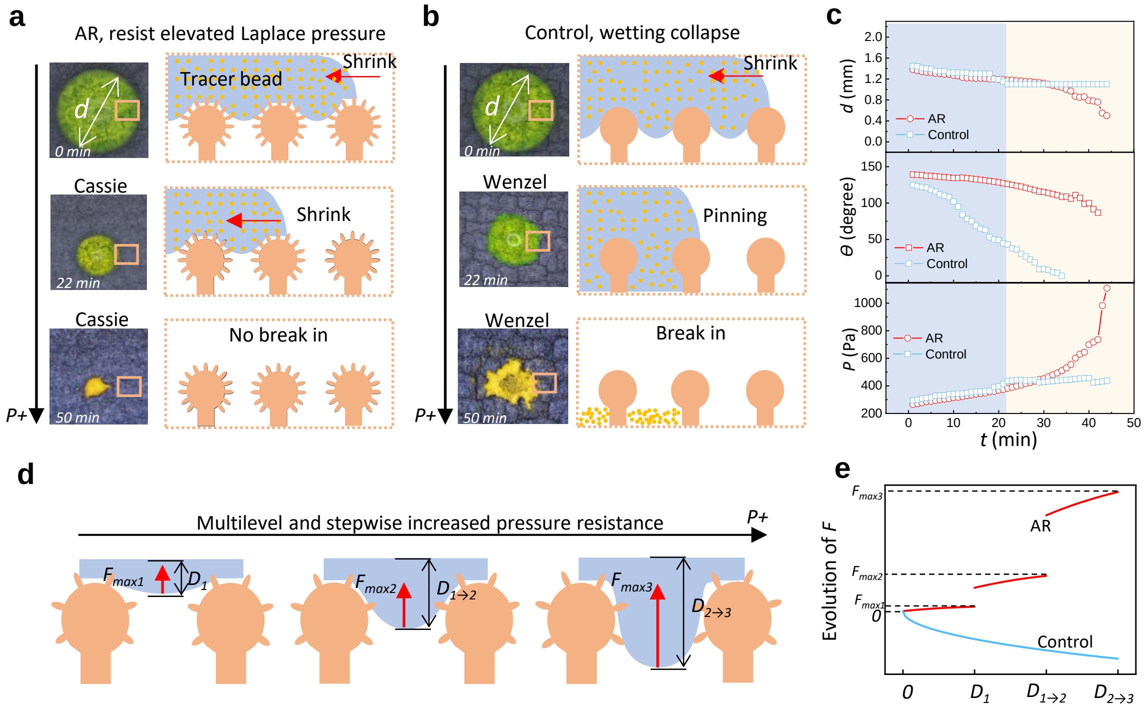

Figure 3. Pressure resistance of the AR surface in stabilizing the Cassie-Baxter state under liquid evaporation. (a, b) Optical images of the evaporating water droplet on the AR surface (a) and control surface (b). Schematics magnifies the box from a side view, which describes the stability of the Cassie-Baxter state, as reflected by the final arrangements of the tracer beads (1 μm diameter) in the liquid droplets. (c) Hydrodynamics during water evaporates on the AR surface and the control surface, including the diameters (d), contact angles (θ), and Laplace pressures (P) of the evaporating drops. Background color differs at t=22 min, corresponding to the time when wetting collapses on the control surface. (d) Schematics illustrating the multilevel and stepwise resistance of the AR surface to liquid invasion caused by the elevated pressure. (e) Stepwise increased F with the development of D.

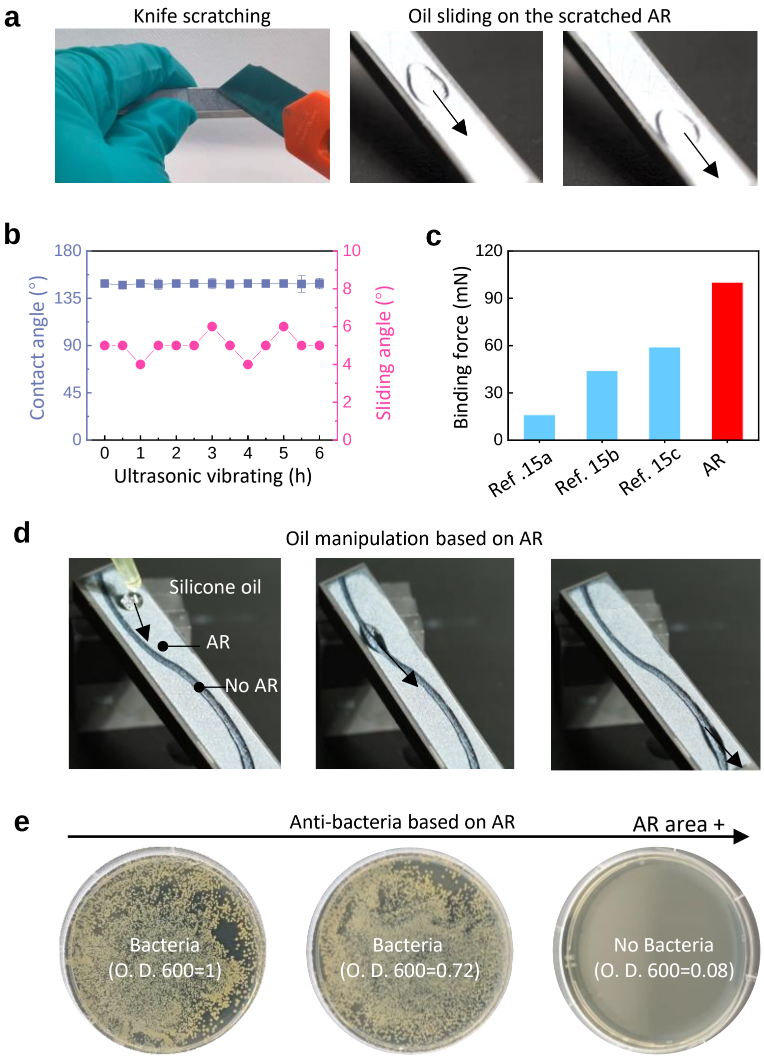

Figure 4. Mechanical robustness of the AR surface and its associated applications. (a) The AR surface allows a silicone oil to slide on the surface after knife scratching. (b) The repellency of the AR surface after ultrasonic cleaning. (c) The binding force of the nanometric reentrants with the AR surface prepared by our method, in comparison to that prepared by the other methods, including MOF[15a], sol-gel[15b] and plasma jet[15c]. (d) Oil manipulation based on the AR surface. The no AR area (S-shaped track) was achieved by selectively removing the AR structures, which is oleophilic. (e) The anti-bacterial performance of the AR surface. With increased AR areas, the bacteria gradually fail to colony the surface. O. D. 600 represents the optical density measured under a wavelength of 600 nm. A higher O. D. 600 value indicates more bacterial colony.